# Operating range of a differential-absorption lidar based on a $CO_2$ laser

M V Ivashchenko, I V Sherstov

**Abstract.** The echolocation range and the remote sensing of ethylene in the atmosphere are simulated for a differential-absorption lidar based on TEA $CO_2$ lasers. The dependence of the lidar echolocation range on the energy and the peak power of probe pulses is shown to be close to logarithmic. It is demonstrated that the use of narrow-band spectral filters is justified only for low-noise detectors and viewing angles of the receiver exceeding 5 mrad. The relative measurement error of the ethylene concentration in the atmosphere is estimated for various detection modes.

## 1. Introduction

In 1994, a prototype of a mobile differential-absorption lidar (DIAL) based on tunable TEA $CO_2$ lasers was designed in the Institute of Atmospheric Optics (IAO), Siberian Division of the Russian Academy of Sciences, Tomsk, Russia. The laser system of this lidar was created in the Institute of Laser Physics (ILP), Siberian Division of the Russian Academy of Sciences, Novosibirsk, Russia. The lidar was installed on a military tractor. The assemblage and the field trials were conducted by a group of IAO and ILP staff members on the premises of the Korean Advanced Institute of Science and Technology (KAIST), Taejon, Republic of Korea [1 – 3]. The group of H J Kong took part in the collaboration from the Korean side [4, 5].

The efforts to create a DIAL with an operating range greater than 10 km have been continued at the ILP. By now, a modernised laser system [6] has been designed and created. It can be used in stationary or mobile versions of the DIAL to conduct large-scale online atmosphere monitoring of large territories. The setup includes two tunable repetitively pulsed TEA $CO_2$ lasers, which emit pairs of optical pulses at 85 lines of the $00^01 – 10^00$ and $00^01 – 02^00$ transitions in the $^{12}C^{16}O_2$ molecule. At 60 lasing lines, the pulse energy exceeds 4 J; at some of the strong lines, the pulse energy reaches 8 – 9 J. A detailed description of the developed lasers is given in Refs [7, 8].

In this work, we analyse the influence of various factors on the echolocation range of the lidar and estimate the range

**M V Ivashchenko, I V Sherstov** Institute of Laser Physics, Siberian Division, Russian Academy of Sciences, prospekt akad. Lavrent'eva 13/3, 630090 Novosibirsk, Russia

of the ethylene sensing in the atmosphere by means of the DIAL based on the developed laser system.

## 2. Basic relationships

Consider a biaxial DIAL whose schematic is shown in Fig. 1. Lasers *1* and *2* emit at the wavelengths $\lambda_1$ and $\lambda_2$, in accordance with the differential absorption technique [9]. The laser beams are made coincident using deflecting mirrors and are directed to the atmosphere with a small time delay between pulses, satisfying the condition of the 'frozen' atmosphere [10]. To control the output power, a fraction of the laser radiation is deflected by NaCl beamsplitter *6* and focused by lens *7* on the sensitive element of control detector *8*. The output collimator *9* forms the probe beams with the required aperture $2a_t$ and divergence $2\theta$. The receiving telescope *5* of the lidar collects the optical echo signals and focuses them on the sensitive element of signal detector *4*. The viewing angle $2\varphi$ of the detector is determined by the aperture dimension and the position of field stop *3*. The separation $b_0$ between the axes of the transceiver and the detector reduces the dynamical range of optical signals received by detector *4*. The effective area of the receiver is determined by the geometric factor of the lidar $G(R)$, which lies between zero and unity [11, 12].
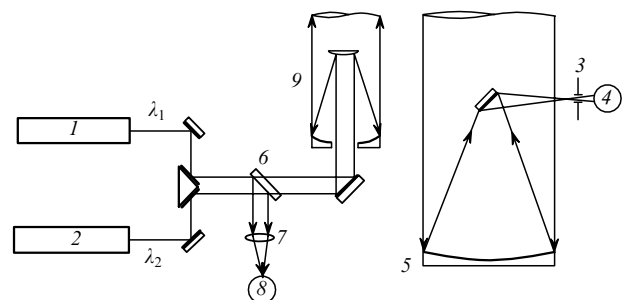


**Figure 1.** Schematic of the differential-absorption lidar: (*1, 2*) tunable TEA $CO_2$ lasers, (*3*) field stop, (*4*) signal detector, (*5*) receiving telescope, (*6*) NaCl beamsplitter, (*7*) lens, (*8*) control detector, (*9*) output collimator.

Consider three possible modes of detection of lidar echo signals. In the first mode, called DAS (differential absorption and scattering) mode [9], the atmospheric aerosol serves as the distributed reflector. Using this mode, one can perform remote, spatially resolved measurements of the profiles of gaseous impurity concentrations in the upper space hemi-

sphere. In the second detection mode, called TT (topographic target) mode, the echo signals diffusely reflected from various topographic objects are detected. In this case, one can accurately measure the average concentrations of gaseous impurities over long paths in certain directions as determined by the topotarget azimuth. The third mode is a special case of the TT mode that is realised when a specular reflector serves as the target; we will call this mode TTR (TT retroreflector). The power of single echo signals detected in the mentioned modes is given by expressions [9, 13]

$$P_{DAS}(R) = \frac{cEK_1K_2\beta_\pi(\lambda)}{2} \left(\frac{A}{R^2}\right) G(R) T^2, \quad (1)$$

$$P_{TT}(R) = PK_1K_2\rho \left(\frac{A}{R^2}\right) G(R) T^2, \quad (2)$$

$$P_{TTR}(R) = \frac{PK_1K_2K_3 d^4}{4\pi(1.22\lambda\theta)^2} \left(\frac{A}{R^4}\right) G(R) T^2, \quad (3)$$

Here, $R$ is the distance; $E$ and $P$ are the energy and the peak power of laser pulses; $c$ is the speed of light; $K_1$, $K_2$, $K_3$ are the optical efficiencies of the lidar transmitter, receiver, and reflector, respectively; $\rho$ is the topotarget reflectance per unit solid angle; $\theta$ is half the angle of divergence of the probe beam; $A$ is the area of the receiving aperture; $d$ is the diameter of the reflector aperture; $\beta_\pi(\lambda)$ is the volume backscatter coefficient of the atmospheric aerosol;

$$T = \exp\left\{ -\int \left[ a_g(\lambda, z) + a_a(\lambda, z) \right] dz \right\}$$

is the atmosphere transmission at the probe wavelength; $a_g$ and $a_a$ are the radiation attenuation coefficients due to absorption by molecular gases and the atmospheric aerosol, respectively.

Consider the signal-to-noise ratio $\varepsilon$ in the regime when single echo signals are detected. The main limiting factor is the shot noise of the detector. In this case, $\varepsilon$ can be written as [13]

$$\varepsilon = \frac{I_s}{\left[2eB(I_s + I_b + I_d)\right]^{1/2}}, \quad (4)$$

where $I_s$ is the signal current of the detector; $I_b$ is the detector current due to the background radiation; $I_d$ is the dark current of the detector; $e$ is the electron charge; and $B$ is the transmission bandwidth of the detector. We can rewrite expression (4) in terms of optical power units using the following well-known expressions [13]

$$S_d = \frac{\eta e}{h\nu}, \quad (5)$$

$$D^* = S_d \left(\frac{A_d}{2eI_d}\right)^{1/2}, \quad (6)$$

$$P_{ne} = \frac{\sqrt{A_d}}{D^*}, \quad (7)$$

$$I_d = \left(\frac{S_d}{D^*}\right)^2 A_d/2e = \left(\frac{P_{ne}\eta e}{h\nu}\right)^2 \bigg/ 2e. \quad (8)$$

Here, $S_d$ is the watt-ampere sensitivity of the detector; $\eta$ is the quantum efficiency of the detector; $h\nu$ is the photon energy; $D^*$ is the detection ability of the detector; $A_d$ is the area of the sensitive element of the detector; and $P_{ne}$ is the equivalent power of the detector noise. Taking into account formulas (4)–(8), $\varepsilon$ assumes the form

$$\varepsilon = \frac{P_s}{\left[2B(P_s + P_b)h\nu/\eta + BP_{ne}^2\right]^{1/2}}. \quad (9)$$

Here, $P_s$ is the power of the received optical signal in the corresponding detection mode; $B_a(\lambda)$ is the luminance of the background radiation; $\Omega = \pi\varphi^2$ is the solid viewing angle of the detector; $\varphi$ is half the viewing angle of the detector; $\Delta\lambda$ is the spectral transmission bandwidth of the detector; and

$$P_b = K_2 B_a(\lambda) A\Omega\Delta\lambda \quad (10)$$

is the power of the background atmospheric radiation that is incident on the detector.

## 3. Numerical simulation

Consider the factors affecting the echolocation range of the lidar in the case of horizontal near the ground propagation paths in the atmosphere. The calculations were performed for the $10P(14)$ transition of the $00^01-10^00$ band of the $^{12}C^{16}O_2$ molecule at $\lambda = 10.53$ μm, which is used for probing ethylene [14, 15]. Table 1 shows the characteristics of the considered DIAL. The output aperture $2a_t$ of the probe beams was chosen to avoid nonlinear absorption of the radiation by the air. According to [16], in this case, the light-field intensity should not exceed $\sim 0.8$ MW cm$^{-2}$ at normal air pressure.

**Table 1.**

| Transmitter | |
|---|---|
| Mode structure of the beam | TEM$_{nm}$ |
| Pulse energy $E$ | 7 J |
| Peak power of radiation pulses $P$ | 70 MW |
| Optical efficiency of the beam shaper $K_1$ | 0.7 |
| Output diameter of the probe beam $2a_t$ | 120 mm |
| Divergence of the probe beam $2\theta$ | 1 mrad |
| Receiver | |
| Diameter of the receiving aperture $2a_r$ | 500 mm |
| Focal length of the telescope $f$ | 1500 mm |
| Viewing angle of the receiver $2\varphi$ | 1.5 mrad |
| Optical efficiency of the receiver $K_2$ | 0.8 |
| Transmission bandwidth of the electronic circuit $B$: | |
|     DAS mode | 1 MHz |
|     TT and TTR modes | 30 MHz |
| Distance between the transmitter and receiver axes $b_0$ | 400 mm |
| Convergence angle $\psi$ of the transmitter and receiver axes | 0 mrad |
| Topotarget and reflector | |
| Topotarget reflectance $\rho$ [23] | 0.01 sr$^{-1}$ |
| Diameter of the reflector aperture $d$ | 150 mm |
| Optical efficiency of the reflector $K_3$ | 0.5 |

The viewing angle of the lidar detector is 1.5 times larger than the divergence of the probe beams. In the simulations, we used the background concentrations of gaseous impurities in the atmosphere and the following parameters of the near ground atmospheric layer at the wavelength 10.53 μm (which are adequate for the summertime at the temperate latitudes):

**Table 2.**

| Detector number | Detector type | Working temperature $/K$ | Detection ability $D^*/cm\ Hz^{1/2}\ W^{-1}$ | Dimension of the sensitive element $/mm$ | $P_{ne}/W\ Hz^{1/2}$ | Spectral transmission bandwidth $\Delta\lambda/\mu m$ |
|---|---|---|---|---|---|---|
| 1 | HgCdTe | 77 | $4 \times 10^{10}$ | 1 | $2.2 \times 10^{-12}$ | 4 |
| 2 | HgMnTe | 77 | $2 \times 10^{11}$ | 0.5 | $2.2 \times 10^{-13}$ | 4 |

the attenuation coefficient due to absorption by molecular gases $\alpha_g = 0.227\ km^{-1}$ [17], the absorption and backscatter coefficients of the atmospheric aerosol $\alpha_a = 0.03047\ km^{-1}$ and $\beta_\pi = 9.967 \times 10^{-5}\ km^{-1}\ sr^{-1}$ [18], respectively, and the background luminance $B_a(\lambda) = 10^{-4}\ W\ cm^{-2}\ sr\ \mu m$ [19].

Table 2 shows the characteristics of the two detectors types (element 4 in Fig. 1) that can be used in the lidar receiver. Detector 1 is an ordinary HgCdTe photodiode cooled by liquid nitrogen; detector 2 is an MMT10-111-0.5 HgMnTe photodiode by Brimrose Corp. of America, which features a higher detection ability.

Fig 2 shows the calculated dependences of the signal-to-noise ratio $\varepsilon$ on the distance $R$ when single lidar echo signals were detected in one of the three echolocation modes (DAS, TT, and TTR) using detector 1 or 2. One can see from the figure that, in the case of detector 2, the echolocation range of the considered lidar at $\varepsilon = 1$ amounts to $\sim 10$ km in the DAS mode (curve 2), $\sim 21$ km in the TT mode (curve 4), and $\sim 40$ km in the TTR mode (curve 6). Note that, in all detection modes, the echolocation range is greater in the case of detector 1 than in the case of detector 2; the effect of the detector $P_{ne}$ is most pronounced in the DAS detection mode (curves 1 and 2).

for the three detection modes, the two detector types, and the rest of the lidar parameters as in Table 1. One can easily see the advantage of using the detector with the lower $P_{ne}$ (detector 2). When detector 1 is used in the DAS or TT modes (curves 1 and 4), the echolocation range remains virtually constant in the viewing angle range from 0.1 to 10 mrad because the main limiting factor is the intrinsic noise of detector 1. If detector 2 is used (curves 2 and 5), a weak dependence of the echolocation range on the viewing angle of the receiver is observed in the range from 0.1 to $2-3$ mrad; after that, the echolocation range decreases with increasing viewing angle.

In the TTR detection mode (curves 7 and 8), the echolocation range decreases with increasing viewing angle because of the reduction in the fraction of the probe beam that is picked up by the reflector. For comparison, Fig. 3 also shows the simulation results when detector 2 is used with a narrow-band spectral filter whose transmission bandwidth is 0.2 μm and the transmission coefficient is 0.5 (curves 3, 6, and 9). One can see that, in all detection modes, the use of the spectral filter is advantageous only for viewing angles greater than 5 mrad; for small viewing angles, it degrades the sensitivity of the lidar receiver.
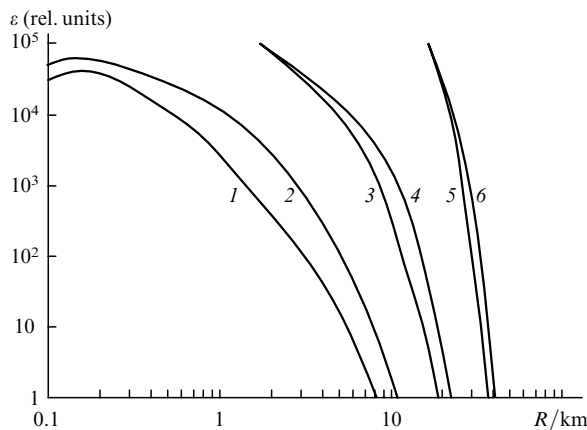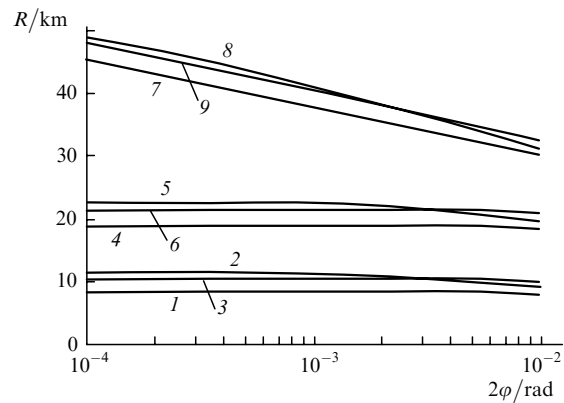


**Figure 2.** Calculated dependences of the signal-to-noise ratio on the echolocation distance in the case when single lidar echo responses are detected in the DAS (1, 2), TT (3, 4), or TTR (5, 6) detection mode using detector 1 (1, 3, 5) or 2 (2, 4, 6).



**Figure 3.** Calculated dependences of the echolocation range on the total viewing angle of the receiver at $\varepsilon = 1$ in the DAS (1, 2, 3), TT (4, 5, 6), and TTR (7, 8, 9) detection modes using detectors 1 (1, 4, 7) and 2 (2, 5, 8), as well as detector 2 with a narrow-band spectral filter (3, 6, 9).

Consider the influence of the receiver viewing angle on the echolocation range. It is known [14] that the use of large viewing angles in lidars reduces the measurement error of gaseous impurity concentrations in the atmosphere. An increase in the viewing angle has no effect on the power of the useful signal but increases the power of the detected background radiation, which affects the value $\varepsilon$ and the sensing range. In the following, we will assume that the ratio of the receiver viewing angle to the probe beam divergence is $\varphi/\theta = 1.5$.

Fig. 3 shows the calculated dependences of the echolocation range on the total viewing angle of the receiver at $\varepsilon = 1$

Consider the influence of the area of the receiver aperture on the sensing range of the lidar. An increase in the area of the receiving telescope leads to an increase in both the useful signal and the background. Fig. 4 shows the calculated dependences of the echolocation range on the area of the receiving telescope at $\varepsilon = 1$ for the three detection modes and the two detectors, including the variant with the spectral filter. The rest of the lidar parameters are as in Table 1. One can see from the figure that, in all detection modes, the echolocation range grows almost logarithmically with the increasing area of the receiving telescope. The significant advantage of using the detector with the lower $P_{ne}$ (detector 2) is easily observable. However, the utilisation of a narrow-band spectral filter

(curves *3*, *6*, and *9*) is fruitless. Note also that, in all detection modes, the increase in the area of the receiving telescope from 0.1 to 1 m² results only in an insignificant increase in the echolocation range: $\sim 24\%$ in the DAS mode (curve *2*), $\sim 13\%$ in the TT mode (curve *5*), and $\sim 8\%$ in the TTR mode (curve *8*).

Consider the influence of the energy characteristics of the probe radiation on the echolocation range of the considered
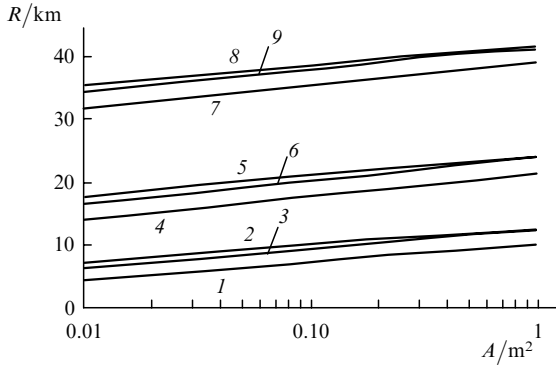


**Figure 4.** Calculated dependences of the echolocation range on the area of the receiving telescope at $\varepsilon = 1$ in the DAS (*1, 2, 3*), TT (*4, 5, 6*), and TTR (*7, 8, 9*) detection modes using detectors 1 (*1, 4, 7*) and 2 (*2, 5, 8*), as well as detector 2 with a narrow-band spectral filter (*3, 6, 9*).
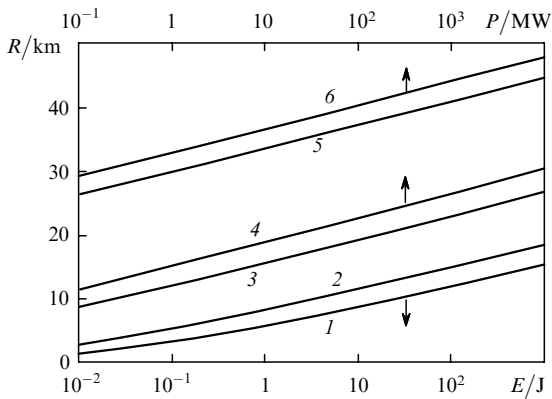


**Figure 5.** Calculated dependences of the echolocation range on the energy and the peak power of probe pulses at $\varepsilon = 1$ in the DAS (*1, 2*), TT (*3, 4*), and TTR (*5, 6*) detection modes using detectors 1 (*1, 3, 5*) and 2 (*2, 4, 6*).

lidar. Fig. 5 shows the calculated dependences of the echolocation range on the energy and the peak power of probe pulses at $\varepsilon = 1$ for the three detection modes, the two detectors, and the rest of the parameters as given in Table 1. The echolocation range increases with increasing energy and peak power of probe pulses in all detection modes. The calculated curves are accurately described by the empirical equation

$$R_i(W) = c_{1i}\,\lg(c_{2i}W + c_{3i}) + c_{4i}. \qquad (11)$$

Here, $R_i$ is the echolocation range at $\varepsilon = 1$; the subscript $i$ denotes the detection mode (DAS, TT, TTR); $W$ is the energy or the peak power of probe pulses; and $c_{1i} - c_{4i}$ are numerical coefficients. In particular, curves *1*, *3*, and *5* in Fig. 5 (detector 1 is used) are described by the following equations with the error $\sim 10\%$

$$R_{\mathrm{DAS}}(E) = 3.14\ \lg(68.3E + 3.47) - 0.0614,$$

$$R_{\mathrm{TT}}(P) = 3.71\lg(3.71 \times 10^3 P + 19.7) + 2.48,$$

$$R_{\mathrm{TTR}}(P) = 3.7\lg(6.16 \times 10^8 P + 1.29 \cdot 10^7) + 2.67,$$

where $R$ is expressed in kilometres; $E$, in joules; and $P$, in megawatts.

Note that, in a wide range of energies and peak powers of probe pulses, one observes a constant difference between the echolocation range corresponding to the cases of detector 2 and detector 1: $\sim 3$ km in the TT (curves *3* and *4*) and the TTR modes (curves *5* and *6*) and from 1.5 to 3 km in the DAS mode (curves *1* and *2*). One can also see from Fig. 5 that, in all detection modes, a ten-fold increase in the pulse energy (from 10 to 100 J) and the peak power (from 100 to 1000 MW) only results in an insignificant increase in the echolocation range: $\sim 30\%$ in the DAS mode (curve *2*), $\sim 15\%$ in the TT mode (curve *4*), and $\sim 10\%$ in the TTR mode (curve *6*). Therefore, the increase in the energy characteristics of the laser with respect to those used in Refs [7, 8] is inexpedient in both mobile and stationary versions of the DIAL.

Consider the influence of attenuation of the radiation in the atmosphere on the sensing range of the lidar. In the above simulations, we used the integrated attenuation coefficient $\alpha = 0.257$ km$^{-1}$, caused by the absorption by molecular gases ($\alpha_{\mathrm{g}}$) and the attenuation by the atmospheric aerosol ($\alpha_{\mathrm{a}}$). However, the published values of $\alpha$ differ: For example, in Ref. [20], $\simeq 0.05 - 0.07$ km$^{-1}$, and in Ref. [15], it is $\sim 0.35$ km$^{-1}$ at various wavelengths. Therefore, it is interesting to analyse the range of the atmosphere sensing for various attenuation coefficients.

Fig. 6 shows the calculated dependences of the lidar echolocation range on the integrated attenuation coefficient for $\varepsilon = 1$ for the three detection modes, the two detectors, and the rest of the parameters as given in Table 1. In the simulations of curves *1* and *2* (DAS mode), the parameter $\beta_{\pi}$ was kept constant. One can see from the figure that detector 2 (curves *2*, *4*, and *6*) offers an advantage over detector 1 (curves *1*, *3*, and *5*). If the atmosphere-induced attenuation $\alpha$ is reduced to 0.1 km$^{-1}$, the echolocation range for the
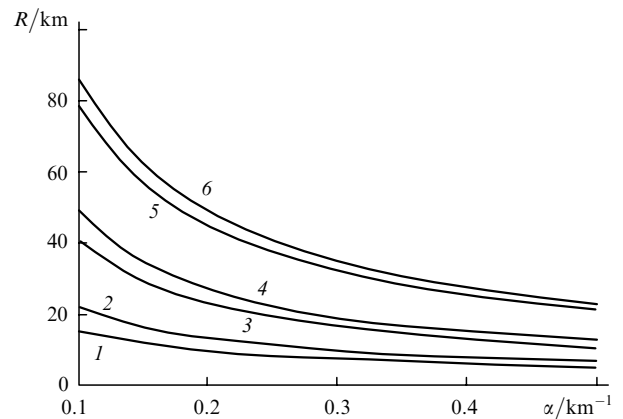


**Figure 6.** Calculated dependences of the echolocation range on the total coefficient of radiation attenuation in the atmosphere at $\varepsilon = 1$ in the DAS (*1, 2*), TT (*3, 4*), and TTR (*5, 6*) detection modes using detectors 1 (*1, 3, 5*) and 2 (*2, 4, 6*).

chosen lidar parameters reaches $\sim$ 21, 49, and 83 km in the DAS, TT, and TTR detection modes, respectively. These estimates generally agree with the range of the SF$_6$ sensing that was achieved in Ref. [20] in the TT detection mode ($\sim$ 16 km). The estimates of the echolocation range in the TTR mode fully coincide with the results of Ref. [20].

Consider the measurement error of the concentration of a gaseous impurity in the atmosphere. If we neglect the variation in the scattering properties of the medium in the wavelength spectral range $\lambda_1 - \lambda_2$ (on line — off line), the expression for the relative error $\delta_N$ [13] can be rewritten as [21]

$$\delta_N = \left[ \frac{\delta_1^2(R) + \delta_1^2(R + \Delta R) + \delta_2^2(R) + \delta_2^2(R + \Delta R)}{n(2\sigma_{13}N\Delta R)^2} \right.$$
$$\left. + \delta_K^2 + \delta_F^2 \right]^{1/2}. \quad (12)$$

Here, $\sigma_{12}$ is the differential absorption coefficient; $N$ is the concentration of the gaseous impurity; $\delta_j = \varepsilon_j^{-1}$ is the relative measurement errors of the power of lidar echo signals; subscripts $j = 1, 2$ refer to the probing at the wavelengths $\lambda_1$ and $\lambda_2$; $n$ is the number of radiation pulses; $\Delta R$ is the spatial resolution; and $\delta_K$ and $\delta_F$ are the relative measurement errors of the differential absorption coefficient and the error induced by the influence of the impurity gases. The last two quantities are systematic errors that are unrelated to the detector noise.
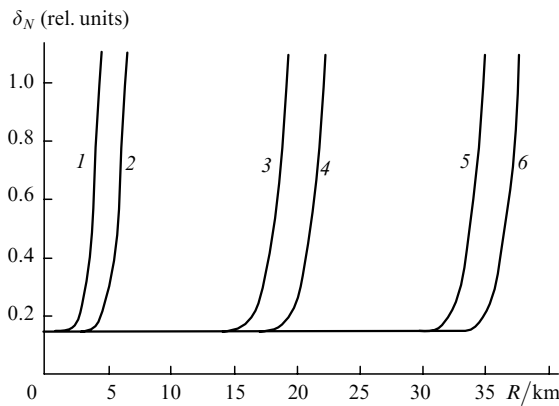


**Figure 7.** Calculated dependences of the relative measurement error of the ethylene concentration in the atmosphere on the echolocation range in the DAS (1, 2), TT (3, 4), and TTR (5, 6) detection modes using detectors 1 (1, 3, 5) and 2 (2, 4, 6). The spatial resolution is $\Delta R = 150$ m (1, 2); the ethylene concentration is $N = 40$ ppb.

Using Eqn. (12), we will now estimate the relative measurement error of the ethylene concentration in the atmosphere. In the calculations, we will assume that $N = 40$ ppb (the doubled background concentration [15]), $\sigma_{12} = 32$ cm$^{-1}$ atm$^{-1}$ for the probing at the wavelengths of the 10$P$(14) and 10$P$(22) lasing transitions of the CO$_2$ laser [10, 15], $n = 10$, the relative error of the measurement of the output laser power by the control detector $\delta_i(R = 0)$ $\sim$ 0.001 (in the TT and TTR detection modes), $\delta_k \sim 0.1$, and $\delta_F \sim 0.1$ [15, 21]. Fig. 7 shows the calculated dependences of the relative measurement error of the ethylene concentration in the atmosphere on the sensing range for the three detection modes and the two detectors. In the calculation of

curves 1 and 2 (the DAS mode), the spatial resolution $\Delta R = 150$ m was chosen in accordance with the duration of probe pulses $\tau_p = 1$ μs [7, 8].

One can see from Fig. 7 that, at small distances, when the lidar echo signals are detected with a high signal-to-noise ratio, the error of the measurement of the ethylene concentration is determined by the errors $\delta_K$ and $\delta_F$. The measurement error of the signal power increases with increasing echolocation distance. The maximum echolocation range, as defined for $\sigma_N = 1$, can be achieved by using detector 2; it amounts to $\sim$ 22 km in the TT mode and $\sim$ 37 km in the TTR mode.

In the DAS detection mode, the error of concentration measurements is mainly determined by the spatial resolution $\Delta R$. Fig. 8 shows the calculated dependences of $\delta_N$ on the echolocation distance for various spatial resolutions in the case when the DAS detection mode and detector 2 are used. For $\Delta R = 15$ and 50 m, we assume that laser pulses are shortened to, respectively, 100 and 300 ns due to the action of the 'plasma shutter' [20, 22]. According to Refs [7, 8], the energy of the shortened pulse decreases to $\sim$ 2.5 J for $\tau_p = 100$ ns ($\sim$ 35% of the initial pulse energy) and $\sim$ 5 J for $\tau_p = 300$ ns ($\sim$ 70% of the initial pulse energy). One can see from Fig. 8 that, in the DAS mode and at $\sigma_N = 1$, the maximum distance of the ethylene sensing ranges from 3 to 7.5 km depending on the spatial resolution $\Delta R$.
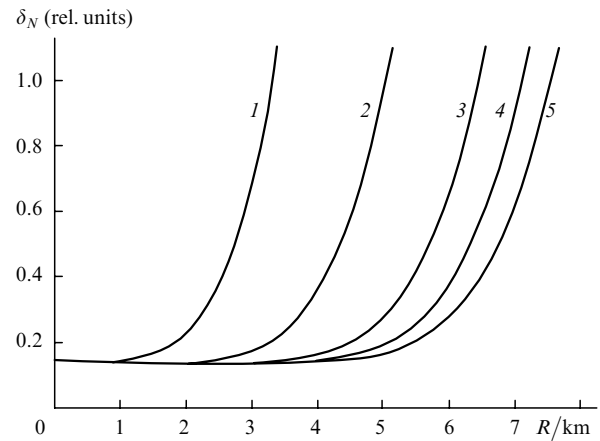


**Figure 8.** Calculated dependences of the relative measurement error of the ethylene concentration in the atmosphere on the echolocation range in the DAS detection mode using detector 2. The ethylene concentration is $N = 40$ ppb, and the spatial resolution is $\Delta R = 15$ (1), 50 (2), 150 (3), 300 (4), and 500 m (5).

## 4. Conclusions

Using numerical simulation, we have estimated the sensing range of the DIAL based on TEA CO$_2$ lasers. The analysis of various factors affecting the lidar echolocation range has demonstrated that, if an ordinary HgCdTe detector is used, the echolocation range in the DAS and TT detection modes is virtually constant in the range of the viewing angle of the receiver from 0.1 to 10 mrad. If one uses a HgMnTe detector, which is characterised by a lower $P_{ne}$, the echolocation range is weakly dependent on the viewing angle of the receiver in the range from 0.1 to 3 mrad. The utilisation of narrow-band spectral filters in the lidars of the considered design is justified only for low-noise detectors and viewing angles of the receiver exceeding 5 mrad.

In all detection modes, the dependence of the lidar echolocation range on the energy and the peak power of probe pulses is close to logarithmic. An increase in the energy and the peak power of laser pulses with respect to what was already realised produces an only insignificant increase in the echolocation range.

Our estimates of the relative measurement error of a gaseous impurity concentration in the atmosphere demonstrated that the considered DIAL makes possible the remote sensing of ethylene over the following distances: from 3 to 7.5 km (subject to the spatial resolution) when detecting the backscattering from the atmospheric aerosol, and up to $\sim 22$ and $\sim 37$ km when detecting the diffuse and specular reflection from a topotarget, respectively.

# References

1. Andreev Yu M, Razenkov I A, Sherstov I V, et al. *Optika Atmosfery i Okeana* **10** 119 (1997) [*Atmospheric and Oceanic Optics* **10** 76 (1997)].
2. Andreev Yu M, Karapuzikov A I, Sherstov I V, et al. *Control and Rehabilitation of Environment* (Tomsk: Spektr, 1998, p. 15).
3. Andreev Y M, Geyko P P, Sherstov I V *SPIE* **3983** 386 (1999).
4. Park Y J, Dho S W, Kong H J *Appl. Opt.* **36** 5158 (1997).
5. Dho S W, Park Y J, Kong H J *Appl. Opt.* **36** 6009 (1997).
6. Karapuzikov A I, Sherstov I V, Malov A N, Ivachenko M V *Proc. SPIE* **4036** 255 (2000).
7. Ivashchenko M V, Karapuzikov A I, Malov A N, Sherstov I V *Prib. Tekh. Eksp.* **41** no. 1 p. 131 (2000) [*Instruments and Experimental Techniques* **43** 119 (2000)].
8. Karapuzikov A I, Malov A N, Sherstov I V *Infrared Phys. Technol.* **41** 77 (2000).
9. Collis R T H, Russell P B, in: *Laser Monitoring of the Atmosphere* (New York: Springer, 1976).
10. Killinger D K, Menyuk N, DeFeo W E *Opt. Lett.* **6** 301 (1981).
11. Halldorsson T, Langerhole J *Appl .Opt.* **17** 240 (1978).
12. Abramochkin A I, Tikhomirov A A *Optika Atmosfery i Okeana* **12** 345 (1999) [*Atmospheric and Oceanic Optics* **12** 331 (1999)].
13. Measures P M *Laser Remote Sensing* (New York: Wiley-Interscience, 1984).
14. Killinger D K, Menyuk N *IEEE J. Quantum Electron.* **17** 1917 (1981).
15. Bondarenko S L, Dolgii S I, Zuev V V, et al. *Optika Atmosfery i Okeana* **5** 611 (1992) [*Atmospheric and Oceanic Optics* **5** 386 (1992)].
16. Ageev B G, Ponomarev Yu N, Tikhomirov B *Nonlinear Opto-Acoustic Spectroscopy of Molecular Gases* (Novosibirsk: Nauka, 1987).
17. Aref'ev V N *Kvantovaya Elektron. (Moscow)* **12** 631 (1985) [*Sov. J. Quantum Electron.* **15** 413 (1985)].
18. Krekov G M, Rakhimov R F *Optical Models of Atmospheric Aerosols* (Tomsk: Tomsk Branch of the Siberian Division of the Academy of Sciences of USSR, 1986).
19. Kriksunov L Z *Handbook of Infrared Technique* (Moscow: Sov. Radio, 1978).
20. Carlisle C B, Laan J E, Carr L W, et al. *Appl. Opt.* **34** 6187 (1995).
21. Zuev V V, Katayev M Yu, Makogon M M, Mitsel' A A *Optika Atmosfery i Okeana* **8** 1136 (1995) [*Atmospheric and Oceanic Optics* **8** 590 (1995)].
22. Kalin A W, Kesselring R, Cao Hongru, Kneubuhl F K *Infrared Phys.* **33** 73 (1992).
23. Berezovskii V V, Splavnik Yu V *Zh. Prikl. Spektrosk.* **40** 805 (1984).